Image-based modeling of hemodynamics in coronary artery aneurysms caused by Kawasaki disease

Dibyendu Sengupta,
Department of Mechanical and Aerospace Engineering, University of California San Diego (UCSD), San Diego, CA, USA

Andrew M. Kahn,
Department of Medicine, University of California San Diego (UCSD), San Diego, CA, USA

Jane C. Burns,
Department of Pediatrics, University of California San Diego (UCSD), San Diego, CA, USA. Rady Children's Hospital San Diego, San Diego, CA, USA

Sethuraman Sankaran,
Department of Mechanical and Aerospace Engineering, University of California San Diego (UCSD), San Diego, CA, USA

Shawn C. Shadden, and
Department of Mechanical, Materials and Aerospace Engineering, IIT, Chicago, IL, USA

Alison L. Marsden
Mechanical and Aerospace Engineering, EBU II–569, University of California San Diego (UCSD), La Jolla, San Diego, CA 92093-0411, USA

Abstract

Kawasaki Disease (KD) is the leading cause of acquired pediatric heart disease. A subset of KD patients develops aneurysms in the coronary arteries, leading to increased risk of thrombosis and myocardial infarction. Currently, there are limited clinical data to guide the management of these patients, and the hemodynamic effects of these aneurysms are unknown. We applied patient-specific modeling to systematically quantify hemodynamics and wall shear stress in coronary arteries with aneurysms caused by KD. We modeled the hemodynamics in the aneurysms using anatomic data obtained by multi-detector computed tomography (CT) in a 10-year-old male subject who suffered KD at age 3 years. The altered hemodynamics were compared to that of a reconstructed normal coronary anatomy using our subject as the model. Computer simulations using a robust finite element framework were used to quantify time-varying shear stresses and particle trajectories in the coronary arteries. We accounted for the cardiac contractility and the microcirculation using physiologic downstream boundary conditions. The presence of aneurysms in the proximal coronary artery leads to flow recirculation, reduced wall shear stress within the aneurysm, and high wall shear stress gradients at the neck of the aneurysm. The wall shear stress

in the KD subject (2.95–3.81 dynes/sq cm) was an order of magnitude lower than the normal control model (17.10–27.15 dynes/sq cm). Particle residence times were significantly higher, taking 5 cardiac cycles to fully clear from the aneurysmal regions in the KD subject compared to only 1.3 cardiac cycles from the corresponding regions of the normal model. In this novel quantitative study of hemodynamics in coronary aneurysms caused by KD, we documented markedly abnormal flow patterns that are associated with increased risk of thrombosis. This methodology has the potential to provide further insights into the effects of aneurysms in KD and to help risk stratify patients for appropriate medical and surgical interventions.

Keywords

Kawasaki disease; Aneurysm; Wall shear stress; Residence time

1 Introduction

Computer simulations of hemodynamics in patient-specific geometries have advanced in recent years and are now being widely used in the study of cardiovascular disease. Simulations provide a means to obtain hemodynamic parameters that cannot be readily obtained by traditional imaging or clinical methods, including flow distribution, wall shear stress, particle residence times, and exercise conditions. Although simulations have played a key role in the study of congenital heart defects (Marsden et al. 2010, 2009; Sundareswaran et al. 2008), abdominal and cerebral aneurysms (Les et al. 2010; Piccinelli et al. 2009), and bypass grafts (Ku et al. 2002), this technology has not been previously applied to patient-specific models of Kawasaki Disease (KD). This study presents the first patient-specific computational simulations of blood flow in a subject with KD using physiologic boundary conditions and a patient-specific model of the aorta and coronary arteries. The downstream boundary condition takes into account the coronary microcirculation and myocardial contractility via a lumped parameter model. We measured the effect of local geometry on velocity patterns, wall shear stress (WSS), oscillatory shear index (OSI), and particle residence times, each of which are postulated to strongly affect the propensity for thrombus formation. By creating a patient-specific virtual control model, we also quantitatively compare and contrast hemodynamics in the aneurysmal and normal coronary artery.

Kawasaki disease (KD) is an acute, self-limited vasculitis occurring primarily in children less than 5 years of age. It is the leading cause of acquired heart disease in children, with over 5,500 cases of KD diagnosed annually in the US alone (Holman et al. 2010). Japan has the highest annual incidence of KD in the world, with 1 in every 185 children affected (Nakamura et al. 2010).

Coronary artery aneurysms occur in roughly 20–25% of untreated KD cases (Kato et al. 1996), and this rate is reduced to 3–5% by treatment with intravenous immunoglobulin (IVIG) within 10 days of fever onset (Newburger et al. 1991). Patients with aneurysms are at increased risk of thrombus formation, myocardial infarction, heart failure, and death (Gordon et al. 2009). In KD patients with aneurysms, there are currently limited clinical data to guide treatments, which could include anti-platelet therapy, systemic anticoagulation,

percutaneous coronary artery interventions, such as stenting or rotational ablation, and coronary artery bypass surgery (Newburger et al. 2004). Since most patients with KD are otherwise healthy, clinicians are faced with the difficult choice of exposing patients to treatment risks, or waiting and watching, knowing that a sudden adverse cardiac event may have serious or even deadly consequences. While aneurysms can be imaged to obtain anatomical information, there are currently no available clinical tools to predict the risk of coronary artery thrombosis or myocardial infarction. Imaging flow in the coronary arteries non-invasively using phase contrast magnetic resonance imaging (MRI) is possible, but is technically challenging because the coronary arteries are small and mobile, with maximum displacements in the right and the left coronary arteries of about 16mm and 10mm, respectively (Hundley et al. 1996; Johnson et al. 2004). CT angiography can now be performed with relatively low radiation doses to non-invasively image coronary artery anatomy (Earls et al. 2008) but provides no hemodynamic information. Despite evidence that hemodynamics, including wall shear stress and flow stagnation, are closely linked to inflammation and risk of thrombosis, clinical decisions are currently typically made based on anatomy alone.

This work builds upon recent advances in simulation technology, including sophisticated lumped parameter boundary conditions (Dubini et al. 1996; Formaggia et al. 2009; Lagana et al. 2002), increasing anatomic realism (Marsden et al. 2010), particle tracking (Shadden and Taylor 2008), and virtual surgery optimization (Yang et al. 2010). Modeling coronary arteries presents particular challenges that are not readily addressed with standard simulation methods. Standard simulation boundary conditions, such as resistance, cannot capture coronary flow and pressure behavior, in which flow and pressure are out of phase. This effect is particularly significant in the left coronary artery (LCA). During systole, the resistance of the coronary bed increases and restricts blood flow through the LCA. During diastole, coronary resistance decreases, and blood flow is maximized. While, in principle, it is possible to model this phenomenon with time-varying impedance boundary conditions, a lack of information on the patient-specific coronary waveform makes the impedance spectrum difficult to obtain. In recent work, novel lumped parameter boundary conditions were developed for modeling coronary flow together with a coupled lumped parameter heart model, which we build upon in the present study (Kim et al. 2010). We also quantify the effects of flow recirculation in the aneurysm by computing particle residence times at locations along both coronary arteries (Lonyai et al. 2010).

In this study, we quantified hemodynamic parameters of likely clinical relevance for assessing the thrombotic risk in a patient with KD, using anatomic data obtained by multi-detector computed tomography (CT). From simulation results, we obtained the first detailed quantitative, time-dependent values of shear stress and residence times using realistic flow conditions in a coronary aneurysm caused by KD. We created a virtual control model by artificially constructing a model of normal coronary anatomy for the same patient to compare normal and pathological hemodynamics.

2 Methods

2.1 Subject data

The subject suffered KD at the age of 3 years. and developed giant coronary artery aneurysms. Anatomic data were obtained from a clinically indicated CT angiogram (64-slice CT General Electric), acquired in 2006 when the patient was 10 years old. The patient has been maintained on warfarin with therapeutic INR between 2.0–2.5 and aspirin (81 mg/day). He currently has no ischemic symptoms. This study was approved by the Institutional Review Board at UCSD, and written subject assent and parent consent were obtained for the imaging and simulation studies.

2.2 Model construction

Four steps were performed to construct patient-specific three-dimensional geometric models from CT image data. These steps were the following: (1) creation of centerline paths in each vessel of interest, (2) segmentation of the vessel lumen using 2D level set methods, (3) lofting the 2D segmentations to create a solid model of the desired vasculature, and (4) meshing of the solid model using unstructured tetrahedral mesh for use in the finite element flow solver. Models are created using a customized version of the open sourced Simvascular software package (Schmidt et al. 2008) (simtk.org).

A virtual control case was created to "heal" the patient by replacing the aneurysmal regions with normal coronary geometry, keeping the rest of the anatomy unchanged. This allowed for the direct comparison of hemodynamic changes between the normal and pathological states. Segmentations in the KD model were manually replaced with circular segmentations in the aneurysmal region only, leaving other segmentations in the model untouched. The diameter and tapering of the segmentations were determined assuming Z-score (normalized diameter) values of 0 and using the body surface area (BSA) of the patient based on the following regression equations (McCrindle et al. 2007)

$$LMCA = 0.31747 \cdot (BSA^{0.36008}) - 0.02887$$
$$pLAD = 0.26108 \cdot (BSA^{0.37893}) - 0.02852$$
$$pRCA = 0.26117 \cdot (BSA^{0.39992}) - 0.02756$$

where LMCA, pLAD, and pRCA represent the left main coronary artery, proximal left anterior descending coronary artery, and proximal right coronary artery, respectively. The above relations were used to prescribe the diameter of the normal coronaries approximately 3–4 cm distal to the ostia. Linear interpolation was used to taper the vessels between this point and normal region distal to the aneurysm. The arch anatomy and coronary geometry distal to the aneurysms were left unchanged, and only the diameter of the proximal aneurysmal regions was changed to the corresponding normal values. The maximum diameters in the aneurysmal regions of the KD model were 1.14 cm in the LAD and 1.08 cm in the RCA, which were almost 3 times the normal values.

2.3 Simulation methods

A finite element mesh was constructed for each model using the commercial software Meshsim (Symmetrix, Inc, Troy, NY). Adaptive meshing was used based on the Hessian of the velocity field, with a minimum mesh size of 0.2 mm to ensure mesh convergence of the solutions (Sahni et al. 2008, 2009). Resulting meshes had over 3.5 million elements for both the normal and the KD model. Simulations were run for 6 cardiac cycles until the pressure fields at the inlet and outlet did not change more than 1% from the previous cycle. Simulations of 6 cardiac cycles took about 26 hours to complete on 60 processors.

A custom stabilized 3-D finite element Navier–Stokes solver was used following our previous work (Vignon-Clementel et al. 2006). The fluids solver and boundary conditions we employ have been thoroughly validated in prior work through in vitro experiments using rigid and compliant physical phantoms, with abdominal aortic aneurysm, patent thoracic artery, and stenotic thoracic artery geometries. Results have shown good agreement between numerically simulated and experimentally measured velocity fields and pressure waveforms in rigid and deformable geometries (Kung et al. 2011a,b).

Blood was modeled as a Newtonian fluid with a density of 1.06 gm/cc and dynamic viscosity of 0.04 dynes/sq cm for all simulations. We assumed the walls to be rigid in all cases. A time-step size of 1ms was chosen to satisfy the stability condition. In order to prevent divergence due to backflow at the outlets of the model, additional stabilization terms were used at the outlet nodes in the fluid solver (Bazilevs et al. 2009; Esmaily et al. 2011), acting only during periods of flow reversal.

2.4 Boundary conditions

Coronary artery downstream boundary conditions are crucial for modeling the physiology of the coronary circulation and microcirculation. Coronary boundary conditions are applied at each coronary outlet of the model, and standard RCR (Windkessel) boundary conditions (Vignon-Clementel et al. 2010) are applied at the outlets of the aorta and branch vessels. Details of the boundary conditions and their implementations are described below.

2.5 Inlet boundary condition

A typical aortic waveform is applied at the inlet of the aorta (Fig. 1), as a Dirichlet boundary condition. The flow waveform is scaled to match the cardiac output and the heart rate of the patient obtained from echocardiographic and clinical data.

2.6 Coronary boundary conditions

Blood flow at the inlet to the coronaries is driven by a combination of the aortic pressure and downstream coronary resistance. However, during systole, the distal coronary resistance increases substantially due to increasing intra-myocardial pressure resulting from the contraction of the heart. The intra-myocardial pressure depends on the aortic flow and ventricular pressures. Hence, there is a complex interaction between the flow at the coronary outlets and the aortic flow at the inlet, which must be captured accurately by the numerical model.

A circuit analogy lumped parameter network (LPN) is constructed to model coronary flow and pressure (Fig. 1) following previous work (Kim et al. 2010). The model is comprised of resistors that model the effect of viscosity and downstream pressure, capacitors that model the vessel compliance, and a time-varying pressure to model the contracting ventricle. This model is governed by a set of ordinary differential equations with a known analytic solution, as described in Appendix I. This equation is implicitly coupled to the coronary outlet boundaries in the finite element solver.

The LPN coronary model has seven parameters that must be tuned to match clinical and literature data. These are the arterial resistance (R_a), microcirculation compliance (C_a), microcirculation resistance ($R_{a-micro}$), myocardial compliance (C_{im}), venous microcirculation resistance ($R_{v-micro}$), venous resistance (R_v), and intra-myocardial pressure ($P_{im}(t)$). All the resistances in the LPN coronary model are in series. The intra-myocardial pressure is determined from the ventricular pressures obtained from a lumped parameter heart model, as described in the next section.

Values of the LPN parameters are first determined for the normal coronary model, and the same values are then applied to the KD model. This choice is justified by the observation that the distal coronary geometry is unaffected in the KD case, and the diameter compares well with normal values. Our methodology to choose parameter values is detailed in the following paragraphs.

The total coronary flow was assumed to be 4% of the cardiac output of the patient (Bogren et al. 1989; Kim et al. 2010), and the flow percentages to the right and left coronaries were chosen to be 40 and 60% of the total coronary flow (Johnson et al. 2008), respectively. The flow split to individual coronary outlet branches in the LCA and RCA was weighted according to the outlet areas.

The total resistance ($R_a + R_{a-micro} + R_{v-micro} + R_v$) at each coronary outlet was initially estimated by the ratio of the mean pressure to the mean flow through that vessel, where the mean blood pressure is determined by (SBP + 2*DBP)/3. SBP and DBP are the systolic and the diastolic blood pressure, respectively, as measured in the clinic.

The relative values of resistances (R_a, $R_{a-micro}$, $R_{v-micro}$ and R_v) and capacitances (C_a and C_{im}) were fixed using literature data (Burattini et al. 1985; Kim et al. 2010). The total resistance and capacitance values for the LCA and RCA were then tuned over multiple flow simulations such that the total coronary flow matched the target values, and the peak systolic to diastolic flow ratio matched typical values for normal patients (Marcus et al. 1999).

2.7 Lumped parameter heart model

The LPN coronary models were connected to a lumped parameter heart model (Kim et al. 2009) on the right and left (Fig. 1) via the intramyocardial pressure. In the heart model, the inductances model inertial effects and the diodes model the valves. The left heart model parameters include the left atrial pressure (P_{LA}), mitral valve, atrio-ventricular valvular resistance (R_{A-V}), atrio-ventricular inductance (L_{A-V}), aortic valve, ventriculo-arterial valvular resistance (R_{V-art}), ventriculo-arterial inductance (L_{A-art}), and left ventricular

pressure. The left ventricular pressure is modeled with a normalized time-varying elastance function (Senzaki et al. 1996). From the normalized elastance function, a patient-specific elastance function is computed from the patient's blood pressure, heart rate, and cardiac output. Parameters in the right heart model are similar.

The intra-myocardial pressure is obtained from the ventricular pressures using appropriate weights, as discussed in Appendix I. The parameter values for the heart model are chosen to match the pulse pressure and the cardiac output of the patient. The patient had a blood pressure of 105/52 and a BSA of 1.16 m^2 at time of scan. His stroke volume, cardiac output, and BSA were 66.8 mL/s, 4.1 L/min and 1.33 m^2, respectively, one year after the scan and were scaled to the time of scan according to the BSA (Dewey et al. 2008), to be 58 mL and 3.4 L/min, respectively. The corresponding cardiac cycle period and heart rate for the patient were 1.02 s and 59 beats per minute. These parameters, along with the applied aortic flow waveform, are used to back out the patient-specific ventricular pressures from an off-line solution of the lumped parameter heart model. The differential equations governing the lumped parameter heart model are given in Appendix I.

2.8 RCR boundary conditions

RCR boundary conditions were applied at all other outlets to model the remaining downstream vasculature. The target mean flow through each outlet was fixed based on the branch area (Zamir et al. 1992). The total resistance of all the outlets was calculated as the ratio of mean pressure to mean flow. The relative values of proximal resistance to total resistance were fixed at 15.6% (Les et al. 2010). The total capacitance values were tuned to match the measured blood pressure of the patient.

2.9 Exposure time computations

A high density of massless particles was injected virtually into in the right and the left coronary artery vasculature, and the particle paths were tracked in the domain following the velocity field. As a measure of particle residence time, the average time spent by the particles in each mesh element was calculated to provide a means to localize and quantify regions of recirculation. Using this procedure, the time spent by all the particles in each element was normalized by the element volume and the total number of particles released, to obtain the cumulative exposure time (CET) (Lonyai et al. 2010). We hypothesize that CET is a clinically significant parameter in quantifying recirculation or stagnation in the flow field. Both vigorously recirculating particles and slow-moving particles contribute to CET, as both increase the likelihood of thrombosis in regions of separated flow. Details of the CET formulation are described in Appendix II.

3 Results

Figure 2 shows the CT data with giant aneurysms in the right and left coronary arteries of the patient and the reconstructed models of both the diseased and the virtually created normal coronary artery models. Simulations were performed with both the virtual control normal model and the diseased KD model using identical boundary conditions.

3.1 Flow and pressure

Figure 3 compares flow and pressure at the outlets of the normal and the diseased coronary arteries. Results confirmed that flow at outlets C and D in the LCA and RCA peaks during diastole, whereas flow at all other outlets peaks during systole. Thus, the boundary conditions have captured the expected physiologic behavior of coronary flow. The high intramyocardial pressure during systole impeded the systolic flow through the coronary arteries, while the low intramyocardial pressure during diastole produced higher flow. The flow and pressure waveforms (Fig. 3) and mean values (Table 1) in the LCA and RCA for the normal and KD cases were nearly identical. The minimum and maximum aortic pressures obtained from the simulation were 106 and 49 mmHg, which compared well with the patient blood pressure of 105/52 mmHg.

3.2 Velocity

The velocity in the left coronary, left circumflex, and the left anterior descending artery was maximum during diastole even when the velocity in all the other branches was much lower (Fig. 4). Velocity in the aneurysms of both the left and right coronaries remained persistently low throughout the cardiac cycle when compared to that of the normal coronary simulation. The flow pattern also exhibited substantial recirculation in the aneurysms.

3.3 Wall shear stress

Wall shear stress and oscillatory shear index (Ku et al. 1985) (OSI) contours are shown in Figs. 5 and 6, respectively. There was a significant reduction in WSS in the aneurysmal parts due to flow recirculation and stagnation (Fig. 5). Values of OSI range from 0 in undisturbed flow with unidirectional shear stress vectors, to 0.5 with disturbed flow and oscillatory shear stress vectors. Flow recirculation led to high values of OSI in the aneurysmal region compared with the normal coronary arteries, where the OSI was almost zero throughout the length of the cardiac cycle (Fig. 6). Thus, the aneurysmal regions experience highly oscillatory and low shear stress compared with the normal model. The time-varying WSS for the normal and KD cases is shown in Fig. 7 for several locations along the length of the LAD and RCA. WSS values varied significantly from the proximal aneurysmal to the distal normal locations throughout the cardiac cycle. By comparison, in the aneurysmal parts of the KD model, the WSS values were nearly an order of magnitude lower than in the normal model. Distal to the aneurysm, there was little difference between the KD and normal WSS curves, confirming that the effect on WSS in the KD case is locally confined. Values in the simulated normal coronary artery models were in the range of previously reported normal values (Giannoglou et al. 2006; Gijsen et al. 2007; Torii et al. 2010). A comparison of WSS at different locations in the KD model showed a significant jump from the aneurysmal to the distal region. (Fig. 8)

The mean, maximum, and minimum values of WSS and OSI in the aneurysmal regions in the LAD and RCA of the KD model are presented in Table 2, together with the corresponding values in the same regions of the normal model. The WSS and OSI values in the normal coronary arteries are about an order of magnitude higher than in the KD model. The OSI in the normal model is nearly zero, indicating nearly unidirectional flow.

Figure 9 compares the spatial and temporal mean WSS and the lumen radius along the length of the RCA and LAD between the KD and the normal model. Distal to the aneurysmal region in the KD model, there is a sudden narrowing of lumen diameter back to normal value. WSS gradients (Lei et al. 2001), which are a measure of the two-dimensional stretch of endothelial cells lining the arterial wall, are also computed. Figure 10 quantifies the spatial and temporal mean WSS, WSS gradients, and OSI vs. radius along the length of the RCA and LAD in the KD model. Due to the narrowing of the lumen radius in the regions distal to the aneurysms, there was a sharp increase in WSS gradient and a drop in OSI. The average WSS gradient increased from 5.50 and 4.85 dynes/cm^3 in the aneurysmal regions of the LAD and RCA, respectively, to 17.50 and 25 dynes/cm^3 at the outlets of the aneurysms. The WSS gradient in the normal coronary artery model over the same region did not fluctuate much, with values of 18.5 dynes/cm^3 in the LAD and 24.40 dynes/cm^3 in the RCA.

3.4 Particle tracking

Particle-tracking simulations performed in the LCA and RCA of the KD model revealed that about 32% of the particles remained in the LCA and 28% remained in the RCA after the first cardiac cycle. Nearly all the particles were flushed out of the domain after 5 cardiac cycles. By comparison, the corresponding simulations performed on the model with normal coronary arteries revealed that only 6% of the particles remained in the LCA and 11% of the particles remained in the RCA after the first cardiac cycle, and all particles in both the LCA and RCA were completely flushed out within just 1.3 cardiac cycles.

The cumulative exposure time (CET) plots at different locations throughout LAD and RCA are shown in Fig. 11. In the aneurysmal region, the CET was high (indicated by red) and progressively decreased with sudden decrease in radius and increasing velocity. We confirmed an inverse relationship between magnitudes of CET and velocity. Figure 12 illustrates the variation of average CET with the lumen radius, indicating that the aneurysmal region had a higher CET compared with the distal region. Increasing CET values along the length of the coronaries also correlated with decreasing WSS values, with correlation coefficients of −0.64 (RCA) and −0.50 (LAD) while decreasing WSS values correlated with larger lumen radius with correlation coefficients of −0.86 (RCA) and −0.77 (LAD) (Fig. 12). The higher values of CET and lower values of WSS indicated substantial flow recirculation in the aneurysmal regions. Distal to the aneurysm, as the WSS suddenly increased, the CET also decreased, as shown in the correlation plots.

4 Discussion

We report the first patient-specific, finite element simulations using custom boundary conditions incorporating clinical data to characterize hemodynamics in aneurysms caused by KD. Simulations revealed highly altered hemodynamic conditions and permitted direct comparison with a virtual control case based on the same patient.

Simulation methods provide a powerful means to obtain quantitative measures of potentially relevant clinical parameters that cannot be readily obtained by conventional imaging modalities. We have demonstrated that modeling with LPN boundary conditions produces realistic physiologic flow conditions in the coronary arteries (Johnson et al. 2008; Marcus et

al. 1999), and that these simulations can provide detailed quantitative data for an individual KD patient. As expected, the presence of aneurysms in our model did not affect the global blood flow and pressure waveforms, since coronary artery resistance is dominated by the distal coronary circulation. However, local parameters related to thrombus formation were strongly affected. Quantitative comparisons of WSS, WSS gradients, OSI, and particle residence times in aneurysms were made between the KD and normal models under physiologic flow conditions. Results showed that WSS is decreased, while WSS gradients, OSI, and residence times are increased in the aneurysmal regions, which is expected due to the sudden increase in lumen radius. These are consistent with increased risk of thrombus formation and inflammation. Although, these results are qualitatively intuitive, the current framework provides a means of quantifying these hemodynamic parameters on a patient-specific basis, values that had not previously been known.

WSS levels were an order of magnitude lower in the aneurysmal region of the KD model compared with the normal model, which were in the range of values previously reported (Giannoglou et al. 2006; Gijsen et al. 2007; Torii et al. 2010). Experiments using rabbit endothelium demonstrated that reduced levels of WSS varying from 0.77 to 2.79 dynes/sq cm were associated with thrombus formation (Sriramarao et al. 1996). Further, results from experiments in parallel plate flow chambers revealed that low shear stress values of 4 dynes/sq cm induced extensive platelet aggregation (Kroll et al. 1996). The mean WSS values for our aneurysm model (2.95–3.81 dynes/sq cm) may well be in a range associated with thrombotic risk. In vitro experimentation to correlate WSS levels with likelihood of thrombosis should be a subject of future investigation.

Compared with the normal model, OSI was an order of magnitude higher in the aneurysmal region of the KD model, indicating increased flow recirculation. In vivo studies using porcine aorta demonstrated that disturbed flow (presumably with elevated OSI) leads to a proinflammatory transcription profile in endothelial cells (Passerini et al. 2004). Additional in vitro studies using bovine endothelial cells revealed that slowly oscillating (1 Hz) shear stress with an amplitude of 3 dynes/sq cm (equal to the upper limit of OSI of 0.5) induced the expression of monocyte chemoattractant protein-1 and increased binding of monocytes to the endothelium (Hwang et al. 2003). Average OSI values (0.08–0.09) in the aneurysmal regions in our simulations were elevated compared with the values in the normal model, which were uniformly zero in the corresponding region. These studies suggest that the combination of these slightly elevated OSI values in the KD model together with low shear values may create conditions sufficient to elicit an inflammatory response and thrombosis.

Results demonstrated that WSS gradients are elevated at the outlet of the aneurysm. Previous work examining WSS gradients has shown that high gradients result in the upregulation of inflammatory markers (Nagel et al. 1999) in endothelial cells, as well platelet aggregation leading to thrombosis (Nesbitt et al. 2009). In vitro experiments demonstrated that localized thrombosis is accompanied by an increase in WSS from 9.6 dynes/sq cm to over 20.4 dynes/sq cm(Nesbitt et al. 2009). This compares favorably to the increase in WSS values from the body of the aneurysm to the outlet in the KD model (3.81 to 12.60 dynes/sq cm in LAD and 2.95 to 14.20 dynes/sq cmin RCA). The simulated levels of WSS and WSS

gradient values support the clinical observation that the aneurysms are prone to thrombosis and inflammation (Samada et al. 2010).

Particle-tracking simulations revealed that 30% of particles re-circulated in the coronary aneurysm for at least one full cardiac cycle, with some particles remaining in the domain for as long as 5 cardiac cycles. This is significantly longer than in the normal coronary artery model, in which all particles were washed from the domain within 1.3 cardiac cycle. CET values, a measure of re-circulation time, were approximately 1.3–2.0 times higher in the aneurysmal region. High values of CET also correlated with regions of low WSS, again suggesting a high risk for thrombosis in these regions. In vitro measurements of particle recirculation and residence times are difficult to taken due to several factors including inaccurate quantification of the number of particles in the model, rapid washing out of particles from the domain, difficulties in accurate measurement of dye recirculation times, and challenges in uniformly seeding the particles without altering the flow field (Wootton and Ku 1999). However, in the present computational method, these problems can be overcome and an accurate representation of the in vivo behavior can be obtained.

The primary focus of this work was to investigate hemodynamic parameters such as WSS, WSSG, OSI, and CET that could inform physicians about risk of thrombus formation and vessel wall inflammation in specific patients. Data from autopsy studies of KD patients demonstrate that thrombosis of aneurysms associated with inflammation in the arterial wall is common (Tanaka et al. 1986). In patients with giant aneurysms such as our subject, there is consensus that systemic anticoagulation reduces morbidity and mortality (Samada et al. 2010). However, in patients with smaller aneurysms (<8 mm), management decisions are less straightforward. The AHA guidelines for the management of KD patients with coronary artery aneurysms were only based on Level of Evidence C (expert opinion, case studies, or standard of care) (Newburger et al. 2004). In addition, there are no quantitative data indicating how the actual shape of the aneurysm affects the clinical risk of thrombus formation. The same techniques presented here could also be applied to patients with smaller aneurysms with a range of shapes. Using this framework, simulated perturbations can be made in the coronary anatomy to systematically study the effects of specific geometric changes on the hemodynamics. Hence, these techniques could provide a framework for evaluating how the size and shape of coronary aneurysms affect the hemodynamics, which would be useful in risk stratifying patients and choosing optimal treatment strategies. Furthermore, these same techniques could also be applied to evaluate coronary artery hemodynamics based upon the anatomic data in patients with other coronary artery pathologies.

Limitations of this work include the assumption of a Newtonian fluid, which could be addressed in future work by the implementation of non-Newtonian models (Johnston et al. 2006) or multiscale modeling of clot formation to predict onset of thrombus (Zhiliang et al. 2008). An additional limitation is the assumption of rigid arterial walls in the simulation, which does not account for the significant motion and curvature changes of the coronary arteries during the cardiac cycle. In addition, the effect of calcium accumulation in the arterial wall that is a frequent sequelae of the inflammation was not considered in our model (Kaichi et al. 2008). This could be addressed in future work through the use of fluid

structure interaction methods, which could be extended to incorporate variable properties of the vessel wall including calcification (Bazilevs et al. 2009). There are limited data on flow split percentages to the left and right coronary arteries and the relationship between the intra-myocardial pressures to the left and right ventricular pressures, and these are possible minor sources of error. For validation of these models, it may be possible to use MRI with phase-contrast imaging to measure coronary artery flow. Another limitation of the current work is the absence of a closed-loop LPN for the inlet and the outlet boundary conditions, which should be implemented in future work. The normal coronary geometry is idealized with a small degree of taper in the virtual control model. It would be useful to compare these results with patient-specific models of normal coronary artery anatomy in the future work. Additionally, particle-tracking simulations may provide an opportunity to correlate clot formation with hemodynamics in future comparisons with in vitro and in vivo data.

In summary, we have utilized patient-specific data to create a simulation framework that allows assessment of velocity, WSS, WSS gradients, OSI, and CET. Future application of this technique will include modeling the effects of arterial wall calcification and aneurysm shape and location on flow dynamics, assessing patient-specific risk for thrombosis, and planning interventions including stent placement and bypass grafting. This work presents a step toward developing such a framework.

Supplementary Material

Refer to Web version on PubMed Central for supplementary material.

Acknowledgments

References

Bazilevs Y, Gohean JR, Hughes TJR, Moser RD, Zhang Y. Patient-specific isogeometric fluid-structure interaction analysis of thoracic aortic blood flow due to implantation of the Jarvik 2000 left ventricular assist device. Comput Methods Appl Mech Eng. 2009; 198(45–46):3534–3550.

Bazilevs Y, Hsu MC, Benson DJ, Sankaran S, Marsden AL. Computational fluid-structure interaction: methods and application to a total cavopulmonary connection. Computat Mech. 2009; 45(1):77–89.

Bogren HG, Klipstein RH, Firmin DN, Mohiaddin RH, Underwood SR, Rees RSO, Longmore DB. Quantitation of antegrade and retrograde blood-flow in the human aorta by magnetic-resonance velocity mapping. Am Heart J. 1989; 117(6):1214–1222. [PubMed: 2729051]

Burattini R, Sipkema P, Vanhuis GA, Westerhof N. Identification of Canine coronary resistance and intramyocardial compliance on the basis of the waterfall model. Ann Biomed Eng. 1985; 13(5): 385–404. [PubMed: 4073625]

Dewey FE, Rosenthal D, Murphy DJ, Froelicher VF, Ashley EA. Does size matter? Clinical applications of scaling cardiac size and function for body size. Circulation. 2008; 117(17):2279–2287. [PubMed: 18443249]

Dubini G, deLeval MR, Pietrabissa R, Montevecchi FM, Fumero R. A numerical fluid mechanical study of repaired congenital heart defects. Application to the total cavopulmonary connection. J Biomech. 1996; 29(6):839–839.

Earls JP, Berman EL, Urban BA, Curry CA, Lane JL, Jennings RS, McCulloch CC, Hsieh J, Londt JH. Prospectively gated transverse coronary CT angiography versus retrospectively gated helical technique: improved image quality and reduced radiation dose. Radiology. 2008; 246(3):742–753. [PubMed: 18195386]

Esmaily MM, Yuri B, Tain-Yen H, Irene V-C, Alison M. MOCHA. A comparison of outlet boundary treatments for prevention of backflow divergence with relevance to blood flow simulations. Computat Mech. 2011 (accepted).

Formaggia L, Quarteroni A, Veneziani A. Cardiovascular mathematics. 2009

Giannoglou GD, Soulis JV, Farmakis TM, Louridas GE. Wall shear stress in normal left coronary artery tree. J Biomech. 2006; 39(4):742–749. [PubMed: 16439244]

Gijsen FJH, Wentzel JJ, Thury A, Lamers B, Schuurblers JCH, Serruys PW, Vander Steen AF. A new imaging technique to study 3-D plaque and shear stress distribution in human coronary artery bifurcations in vivo. J Biomech. 2007; 40(11):2349–2357. [PubMed: 17335832]

Gordon JB, Kahn AM, Burns JC. When children with kawasaki disease grow up myocardial and vascular complications in adulthood. J Am College Cardiol. 2009; 54(21):1911–1920.

Holman RC, Belay ED, Christensen KY, Folkema AM, Steiner CA, Schonberger LB. Hospitalizations for Kawasaki Syndrome Among Children in the United States, 1997–2007. Pediatric Infect Disease J. 2010; 29(6):483–488.

Hundley WG, Lange RA, Clarke GD, Meshack BM, Payne J, Landau C, McColl R, Sayad DE, Willett DL, Willard JE, et al. Assessment of coronary arterial flow and flow reserve in humans with magnetic resonance imaging. Circulation. 1996; 93(8):1502–1508. [PubMed: 8608617]

Hwang J, Ing MH, Salazar A, Lassegue B, Griendling K, Navab M, Sevanian A, Hsiai TK. Pulsatile versus oscillatory shear stress regulates NADPH oxidase subunit expression—implication for native LDL oxidation. Circulat Res. 2003; 93(12):1225–1232. [PubMed: 14593003]

Johnson K, Sharma P, Oshinski J. Coronary artery flow measurement using navigator echo gated phase contrast magnetic resonance velocity mapping at 3. 0 T. J Biomech. 2008; 41(3):595–602. [PubMed: 18036532]

Johnson KR, Patel SJ, Whigham A, Hakim A, Pettigrew RI, Oshinski JN. Three-dimensional, time-resolved motion of the coronary arteries. J Cardiovasc Magnet Resonan. 2004; 6(3):663–673.

Johnston BM, Johnston PR, Corney S, Kilpatrick D. Non-Newtonian blood flow in human right coronary arteries: transient simulations. J Biomech. 2006; 39(6):1116–1128. [PubMed: 16549100]

Kaichi S, Tsuda E, Fujita H, Kurosaki K, Tanaka R, Naito H, Echigo S. Acute coronary artery dilation due to Kawasaki disease and subsequent late calcification as detected by electron beam computed tomography. Pediatr Cardiol. 2008; 29(3):568–573. [PubMed: 18043859]

Kato H, Sugimura T, Akagi T, Sato N, Hashino K, Maeno Y, Kazue T, Eto G, Yamakawa R. Long-term consequences of Kawasaki disease—a 10- to 21-year follow-up study of 594 patients. Circulation. 1996; 94(6):1379–1385. [PubMed: 8822996]

Kim HJ, Vignon-Clementel IE, Coogan JS, Figueroa CA, Jansen KE, Taylor CA. Patient-specific modeling of blood flow and pressure in human coronary arteries. Ann Biomed Eng. 2010; 38(10): 3195–3209. [PubMed: 20559732]

Kim HJ, Vignon-Clementel IE, Figueroa CA, LaDisa JF, Jansen KE, Feinstein JA, Taylor CA. On coupling a lumped parameter heart model and a three-dimensional finite element aorta model. Ann Biomed Eng. 2009; 37(11):2153–2169. [PubMed: 19609676]

Kroll MH, Hellums JD, McIntire LV, Schafer AI, Moake JL. Platelets and shear stress. Blood. 1996; 88(5):1525–1541. [PubMed: 8781407]

Ku DN, Giddens DP, Zarins CK, Glagov S. Pulsatile flow and atherosclerosis in the human carotid bifurcation—positive correlation between plaque location and low oscillating shear-stress. Arteriosclerosis. 1985; 5(3):293–302. [PubMed: 3994585]

Ku JP, Draney MT, Arko FR, Lee WA, Chan FP, Pelc NJ, Zarins CK, Taylor CA. In vivo validation of numerical prediction of blood flow in arterial bypass grafts. Ann Biomed Eng. 2002; 30(6):743–752. [PubMed: 12220075]

Kung EO, Les AS, Figueroa CA, Medina F, Arcaute K, Wicker RB, McConnell MV, Taylor CA. In vitro validation of finite element analysis of blood flow in deformable models. Ann Biomed Eng. 2011a; 39(7):1947–1960. [PubMed: 21404126]

Kung EO, Les AS, Medina F, Wicker RB, McConnell MV, Taylor CA. In vitro validation of finite-element model of AAA hemodynamics incorporating realistic outlet boundary conditions. J Biomech Eng Trans Asme. 2011b; 133(4)

Lagana K, Dubini G, Migliavacca F, Pietrabissa R, Pennati G, Veneziani A, Quarteroni A. Multiscale modelling as a tool to prescribe realistic boundary conditions for the study of surgical procedures. Biorheology. 2002; 39(3–4):359–364. [PubMed: 12122253]

Lei M, Giddens DP, Jones SA, Loth F, Bassiouny H. Pulsatile flow in an end-to-side vascular graft model: comparison of computations with experimental data. J Biomech Eng Trans Asme. 2001; 123(1):80–87.

Les AS, Shadden SC, Figueroa CA, Park JM, Tedesco MM, Herfkens RJ, Dalman RL, Taylor CA. Quantification of hemodynamics in abdominal aortic aneurysms during rest and exercise using magnetic resonance imaging and computational fluid dynamics. Ann Biomed Eng. 2010; 38(4): 1288–1313. [PubMed: 20143263]

Lonyai A, Dubin A, Feinstein J, Taylor C, Shadden S. New insights into pacemaker lead-induced venous occlusion: simulation-based investigation of alterations in venous biomechanics. Cardiovasc Eng. 2010; 10(2):84–90. [PubMed: 20514553]

Marcus JT, Smeenk HG, Kuijer JPA. Flow profiles in the left anterior descending and the right coronary artery assessed by MR velocity quantification: effects of through-plane and in-plane motion of the heart. J Comput Assist Tomography. 1999; 23(4):567–576.

Marsden A, Reddy V, Shadden S, Chan F, Taylor C, Feinstein J. A new multiparameter approach to computational simulation for Fontan assessment and redesign. Congenit Heart Dis. 2010; 5(2): 104–117. [PubMed: 20412482]

Marsden AL, Bernstein AJ, Reddy VM, Shadden SC, Spilker RL, Chan FP, Taylor CA, Feinstein JA. Evaluation of a novel Y-shaped extracardiac Fontan baffle using computational fluid dynamics. J Thorac Cardiovasc Surg. 2009; 137(2):394–U187. [PubMed: 19185159]

McCrindle BW, Li JS, Minich LL, Colan SD, Atz AM, Takahashi M, Vetter VL, Gersony WM, Mitchell PD, Newburger JW, et al. Coronary artery involvement in children with Kawasaki disease—risk factors from analysis of serial normalized measurements. Circulation. 2007; 116(2):174–179. [PubMed: 17576863]

Nagel T, Resnick N, Dewey CF, Gimbrone MA. Vascular endothelial cells respond to spatial gradients in fluid shear stress by enhanced activation of transcription factors. Arteriosclerosis Thrombosis Vascular Biol. 1999; 19(8):1825–1834.

Nakamura Y, Yashiro M, Uehara R, Sadakane A, Chihara I, Aoyama Y, Kotani K, Yanagawa H. Epidemiologic features of Kawasaki Disease in Japan: results of the 2007–2008 nationwide survey. J Epidemiol. 2010; 20(4):302–307. [PubMed: 20530917]

Nesbitt WS, Westein E, Tovar-Lopez FJ, Tolouei E, Mitchell A, Fu J, Carberry J, Fouras A, Jackson SPA. Shear gradient-dependent platelet aggregation mechanism drives thrombus formation. Nat Med. 2009; 15(6):665–U146. [PubMed: 19465929]

Newburger JW, Takahashi M, Beiser AS, Burns JC, Bastian J, Chung KJ, Colan SD, Duffy CE, Fulton DR, Glode MP, et al. A single intravenous-infusion of gamma-globulin as compared with 4 infusions in the treatment of acute Kawasaki syndrome. New England J Med. 1991; 324(23):1633–1639. [PubMed: 1709446]

Newburger JW, Takahashi M, Gerber MA, Gewitz MH, Tani LY, Burns JC, Shulman ST, Bolger AF, Ferrieri P, Baltimore RS, et al. Diagnosis, treatment, and long-term management of Kawasaki disease - A statement for health professionals from the committee on rheumatic fever, endocarditis and Kawasaki disease, council on cardiovascular disease in the young, American Heart Association. Circulation. 2004; 110(17):2747–2771. [PubMed: 15505111]

Passerini AG, Polacek DC, Shi CZ, Francesco NM, Manduchi E, Grant GRm, Pritchard WF, Powell S, Chang GY, Stoeckert CJ, et al. Coexisting proinflammatory and antioxidative endothelial transcription profiles in a disturbed flow region of the adult porcine aorta. Proc Natl Acad Sci USA. 2004; 101(8):2482–2487. [PubMed: 14983035]

Piccinelli M, Veneziani A, Steinman DA, Remuzzi A, Antiga L. A framework for geometric analysis of vascular structures: application to cerebral aneurysms. Ieee Trans Med Imaging. 2009; 28(8): 1141–1155. [PubMed: 19447701]

Sahni O, Jansen KE, Shephard MS, Taylor CA, Beall MW. Adaptive boundary layer meshing for viscous flow simulations. Eng Comput. 2008; 24(3):267–285.

Sahni O, Jansen KE, Taylor CA, Shephard MS. Automated adaptive cardiovascular flow simulations. Eng Comput. 2009; 25(1):25–36.

Samada K, Shiraishi H, Sato A, Momoi MY. Grown-up Kawasaki disease patients who have giant coronary aneurysms. World J Pediatr. 2010; 6(1):38–42. [PubMed: 20143209]

Schmidt JP, Delp SL, Sherman MA, Taylor CA, Pande VS, Altman RB. The Simbios national center: systems biology in motion. Proc Ieee. 2008; 96(8):1266–1280.

Senzaki H, Chen CH, Kass DA. Single-beat estimation of endsystolic pressure-volume relation in humans—a new method with the potential for noninvasive application. Circulation. 1996; 94(10): 2497–2506. [PubMed: 8921794]

Shadden SC, Taylor CA. Characterization of coherent structures in the cardiovascular system. Ann Biomed Eng. 2008; 36(7):1152–1162. [PubMed: 18437573]

Sriramarao P, Languino LR, Altieri DC. Fibrinogen mediates leukocyte-endothelium bridging in vivo at low shear forces. Blood. 1996; 88(9):3416–3423. [PubMed: 8896406]

Sundareswaran KS, Pekkan K, Dasi LP, Whitehead K, Sharma S, Kanter KR, Fogel MA, Yoganathan AP. The total cavopulmonary connection resistance: a significant impact on single ventricle hemodynamics at rest and exercise. Am J Physiol Heart Circulat Physiol. 2008; 295(6):H2427–H2435.

Tanaka N, Naoe S, Masuda H, Ueno T. Pathological-study of sequelae of Kawasaki-Disease (MCLS) —with special reference to the heart and coronary arterial lesions. Acta Pathol Jpn. 1986; 36(10): 1513–1527. [PubMed: 3799188]

Torii R, Keegan J, Wood NB, Dowsey AW, Hughes AD, Yang G-Z, Firmin DN, Thom SAM, Xu XY. MR image-based geometric and hemodynamic investigation of the right coronary artery with dynamic vessel motion. Ann Biomed Eng. 2010; 38(8)

Vignon-Clementel IE, Figueroa CA, Jansen KE, Taylor CA. Outflow boundary conditions for three-dimensional finite element modeling of blood flow and pressure in arteries. Comput Methods Appl Mech Eng. 2006; 195(29–32):3776–3796.

Vignon-Clementel IE, Figueroa CA, Jansen KE, Taylor CA. Outflow boundary conditions for 3Dsimulations of non-periodic blood flow and pressure fields in deformable arteries. Comput Methods Biomech Biomed Eng. 2010; 13(5)

Wootton DM, Ku DN. Fluid mechanics of vascular systems, diseases, and thrombosis. Annu Rev Biomed Eng. 1999; 1:299–329. [PubMed: 11701491]

Yang WG, Feinstein JA, Marsden AL. Constrained optimization of an idealized Y-shaped baffle for the Fontan surgery at rest and exercise. Comput Methods Appl Mech Eng. 2010; 199(33–36):2135–2149.

Zamir M, Sinclair P, Wonnacott TH. Relation between diameter and flow in major branches of the arch of the aorta. J Biomech. 1992; 25(11):1303–1310. [PubMed: 1400531]

Zhiliang X, Nan C, Kamocka MM, Rosen ED, Alber M. A multiscale model of thrombus development. J R Soc Interf. 2008:705–722.

Appendix I

This appendix provides the equations for the lumped parameter boundary conditions that were coupled to the finite element flow solver, following previous work (Lonyai et al. 2010). First, the equations for the lumped parameter heart model are provided. The heart model was used off-line to provide intra-myocardial pressure information for the lumped parameter coronary boundary conditions. Second, the lumped parameter coronary boundary conditions are described in detail.

Heart model

Phase I

t = 0 to t_1—isovolumetric contraction (Valve 1 and valve 2 closed)

$$\frac{dQ_1}{dt} = 0$$
$$\frac{dV_V}{dt} = 0$$

$$P_V(t) = E(t)(V_V(t) - V_0)$$

Phase II

t = t_1 to t_2—ejection (Valve 1 closed and valve 2 open)

$$\frac{dQ_1}{dt} = 0$$
$$\frac{dV_V}{dt} = -Q_a$$

$$P_v(t) = E(t)(V_V(t) - V_0)$$

Phase III

t = t_2 to t_3—isovolumetric relaxation (Valve 1 and valve 2 closed)

$$\frac{dQ_1}{dt} = 0$$
$$\frac{dV_v}{dt} = 0$$

$$P_v(t) = E(t)(V_v(t) - V_0)$$

Phase IV

t = t_3 to t_4—filling (Valve 1 open and valve 2 closed)

$$\frac{dQ_1}{dt} = \frac{1}{L_{AV}}[P_A - R_{AV}Q_1(t) - E(t)(V_V(t) - V_0)]$$
$$\frac{dV_V}{dt} = -Q_1(t)$$

$$P_V(t) = E(t)(V_V(t) - V_0)$$

In the above equations, E(t) is the patient-specific elastance function, $Q_1(t)$ is the flow rate through valve 1, $V_V(t)$ is the ventricular blood volume, $P_V(t)$ is the ventricular pressure, P_A

is the atrial pressure, R_{AV} is the atrio-ventricular valvular resistance, and L_{AV} is the ventriculo-arterial inductance.

Valve 1 is open when $P_A > P_V(t)$ and is closed when $P_A \leq P_V(t)$.

Valve 2 is open when $Q_A > 0$ and $\frac{dQ_A}{dt} > 0$ and is closed when $Q_A = 0$ and $\frac{dQ_A}{dt} < 0$ where Q_A is the flow rate through valve 2.

The Intra-myocardial pressure is $P_{im}(t) = \lambda_1 P_{LV}(t) + \lambda_2 P_{RV}(t)$ where $P_{LV}(t)$ and $P_{RV}(t)$ represent the pressure of the left and the right ventricles, respectively.

For the left coronary artery outlets, $\lambda_1 = 1.0$ and $\lambda_2 = 0.0$, since these outlets supply blood only to the left ventricle. However, the right coronary arteries supply blood to both the right and left ventricles, with the longest branch of the RCA supplying blood to the left ventricle, and the others supplying the right ventricle. The weights of the myocardial pressure for the right coronary artery outlets are therefore calculated based on the outlet areas of the branches in the RCA, resulting in a right/left perfusion ratio of approximately 7:3 (i.e. $\lambda_1 = 0.3$ and $\lambda_2 = 0.7$). Figure 13 shows the right and the left ventricular pressures, as well as the pressure volume loop for the patient under consideration.

Coronary boundary condition

In the finite element solver, the coronary boundary condition couples the pressure $P(t)$ with the flow rate $Q(t)$ at the coronary outlet boundaries through the following equation using the coupled multi-domain method of Vignon-Clementel et al. (2006) as implemented in the work of Kim et al. (2010)

$$
\begin{aligned}
P(t) = & \left(RQ(t) + \int_0^t e^{\lambda_1(t-s)} Z_1 Q(s) ds \right) \\
& - \int_0^t e^{\lambda_2(t-s)} Z_2 Q(s) ds + \left(Ae^{\lambda_1 t} - Be^{\lambda_2 t} \right) \\
& + \left(\int_0^t e^{\lambda_1(t-s)} Y_2 P_{im}(s) ds - \int_0^t e^{\lambda_2(t-s)} Y_2 P_{im}(s) ds \right)
\end{aligned}
$$

where

$$
\lambda_1 = \frac{-p_1 + \sqrt{p_1^2 - 4 P_0 P_2}}{2 P_2}
$$

$$
\lambda_2 = \frac{-p_1 - \sqrt{p_1^2 - 4 P_0 P_2}}{2 P_2}
$$

$$
A = \frac{-1}{\sqrt{p_1^2 - 4 p_0 P_2}} \left[(q_2 \lambda_1 + q_1) Q(0) + q_2 \frac{dQ}{dt}(0) + b_1 P_{im}(0) + p_2 \left(\lambda_2 P(0) - \frac{dP}{dt}(0) \right) \right]
$$

$$B = \frac{-1}{\sqrt{p_1^2 - 4p_0 p_2}} \left[(q_2 \lambda_2 + q_1) Q(0) + q_2 \frac{dQ}{dt}(0) + b_1 P_{im}(0) + p_2 \left(\lambda_1 P(0) - \frac{dP}{dt}(0) \right) \right]$$

$$R = \frac{q_2}{P_2}$$

$$Z_1 = \frac{q_2 \lambda_1^2 + q_1 \lambda_1 + q_0}{\sqrt{p_1^2 - 4p_0 p_2}}$$

$$Z_2 = \frac{q_2 \lambda_2^2 + q_1 \lambda_2 + q_0}{\sqrt{p_1^2 - 4p_0 p_2}}$$

$$Y_1 = \frac{b_1 \lambda_1 + b_0}{\sqrt{p_1^2 - 4p_0 p_2}}$$

$$Y_2 = \frac{b_1 \lambda_1 + b_0}{\sqrt{p_1^2 - 4p_0 p_2}}$$

$$p_0 = 1$$

$$p_1 = R_{a-micro} \, C_a + (R_V + R_{V-micro}) \, (C_a + C_{im})$$

$$p_2 = C_a \, C_{im} \, R_{a-micro} \, (R_V + R_{V-micro})$$

$$q_0 = R_a + R_{a-micro} + R_V + R_{V-micro}$$

$$q_1 = R_a \, C_a \, (R_{a-micro} + R_V + R_{V-micro}) + C_{im} \, (R_a + R_{a-micro}) \, (R_V + R_{V-micro})$$

$$q_2 = C_a \, C_{im} \, R_a \, R_{a-micro} \, (R_V + R_{V-micro})$$

$$b_0 = 0$$

$$b_1 = C_{im} \, (R_V + R_{V-micro})$$

Appendix II

Equations for Cumulative Exposure Time (CET)

For an isotropic tetrahedral mesh, CET is computed at each element e based on the following equation

$$\mathrm{CET}_e = \frac{1}{N_t V_e} \sum_{p=1}^{N_t} \int_0^\infty H_e^p(t) \, dt$$

where

V_e is the volume of the tetrahedral element e

N_t is the total number of particles released in the domain

$$H_e^p(t) = \begin{cases} 1 & \text{if particle p is inside element e} \\ 0 & \text{otherwise} \end{cases}$$

In the case of an anisotropic mesh, as in the present study, CET is scaled with the average length of the tetrahedral elements, and the volume V_e is replaced by the cube root of V_e.

To achieve adequate resolution in the CET computation, particle tracking was performed with over 10 million particles in the right and the left coronary arteries in each cardiac cycle. Particles were released once at the start of simulation, and particle tracking continued until all the particles were washed from the domain.
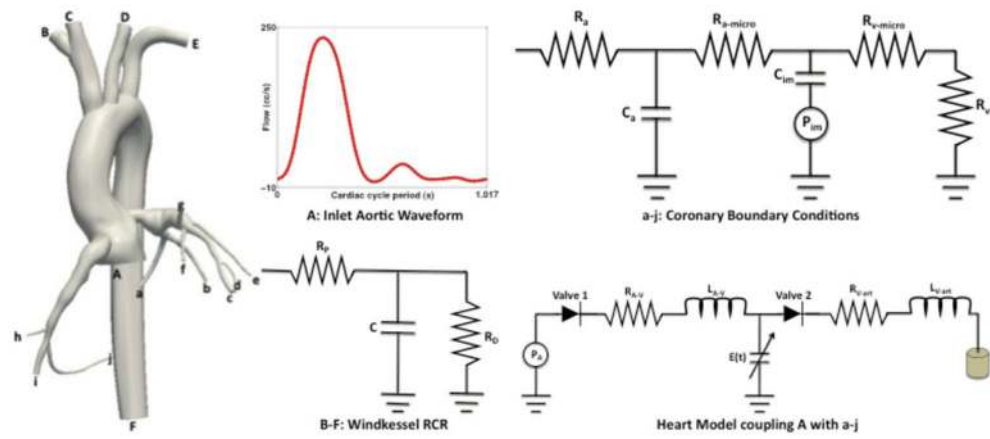
Fig. 1.
Boundary conditions imposed at the inlet (*A*) and outlet (*F*) of the aorta, the outlets of the aortic branches (*B–E*), and the outlets of the left and right coronary arteries (*a–j*), which are coupled to the lumped parameter heart model shown. The waveform shown is imposed on the aortic inlet
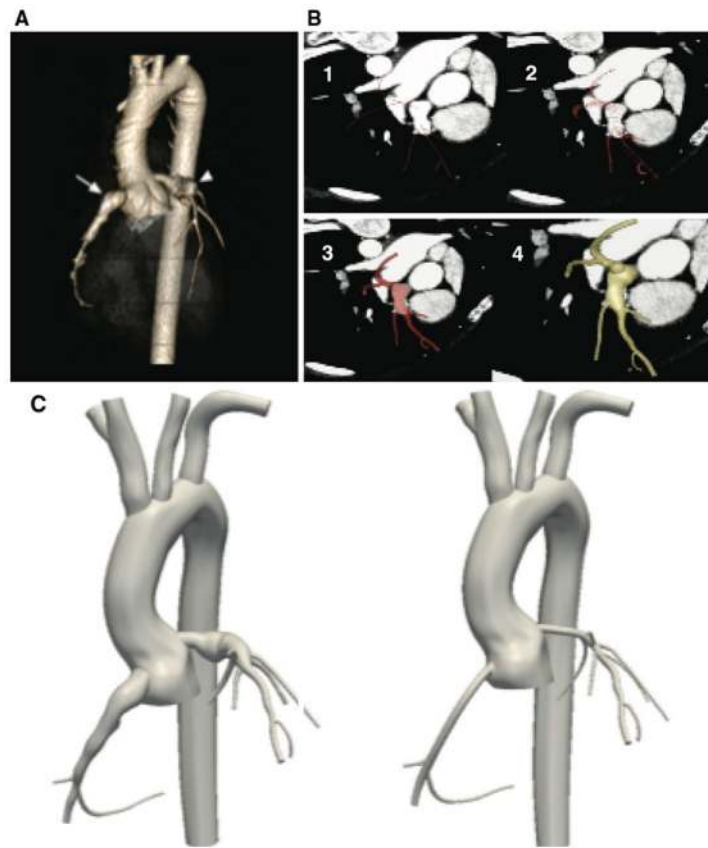
Fig. 2.
Image data and model construction for a 10-year-old KD patient: **A** Three-dimensional reconstruction of CT data showing giant aneurysms of the proximal right (*arrow*) and left main and proximal left anterior descending (*arrowhead*) coronary arteries. **B** Four steps of model construction are 1) Creating paths, 2) Creating segmentations, 3) Lofting geometry, and 4) Meshing **C** KD patient-specific model (*left*) and virtual control constructed from the same data (*right*)
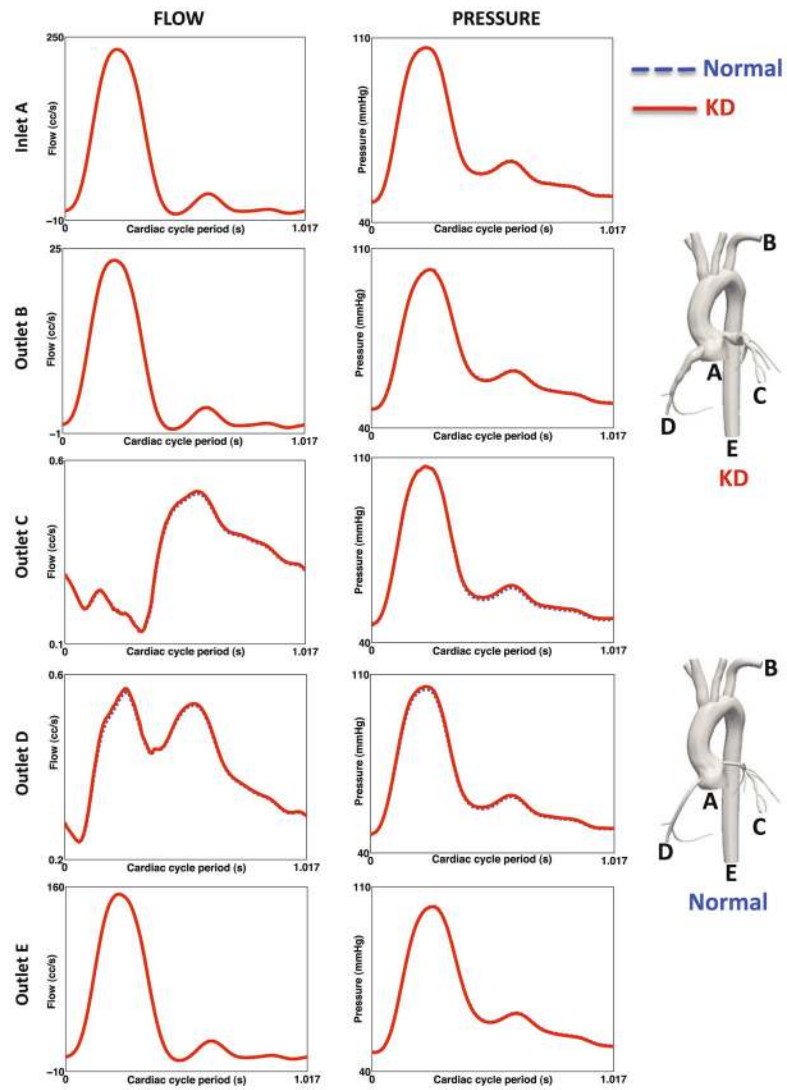
Fig. 3.
Flow and pressure waveform comparison for the normal and KD model over one cardiac cycle at different outlets. The aneurysmal geometry results in no significant changes to aortic or coronary flow and pressure compared with the normal case
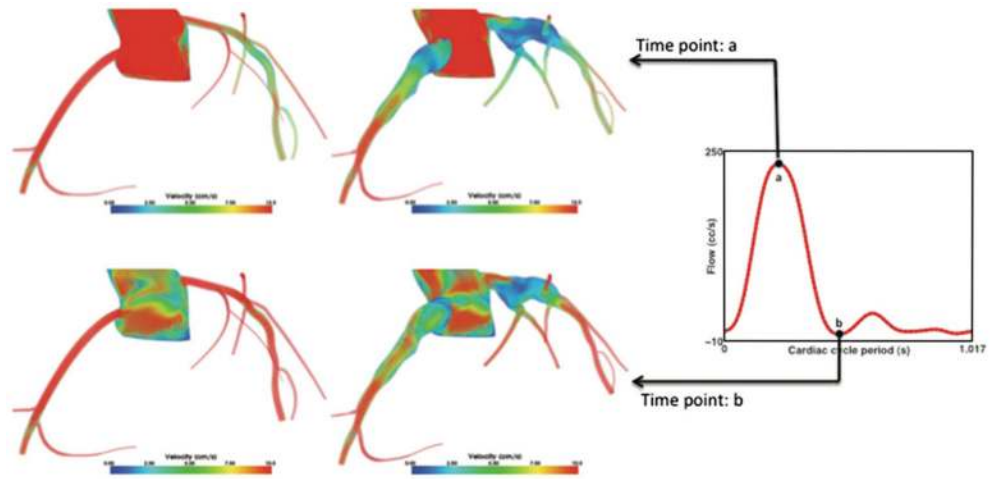
Fig. 4.
Comparison of volume rendered velocity at different points in the cardiac cycle for the KD and normal models. Flow stagnation is evident in the KD model throughout the cardiac cycle. Magnified view of the coronary arteries is shown
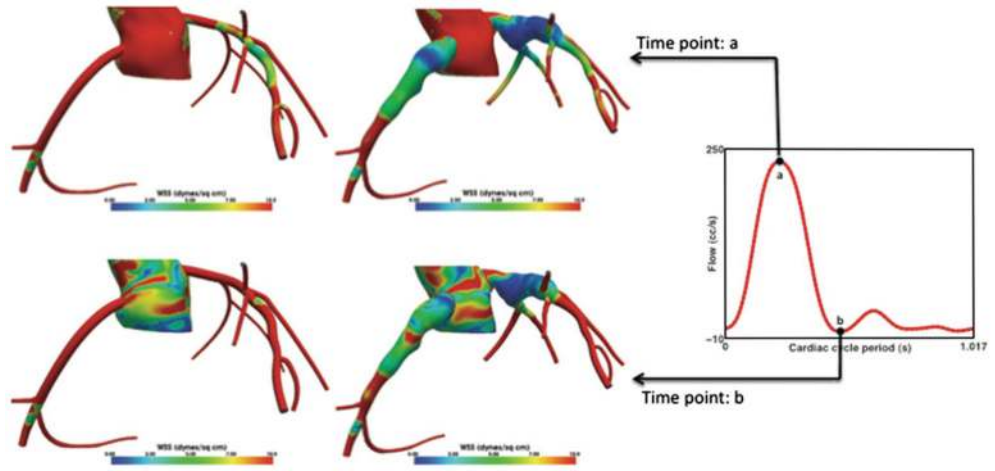
Fig. 5.

Comparison of WSS at different points in the cardiac cycle for the KD and normal models.
Magnified view of the coronary arteries is shown
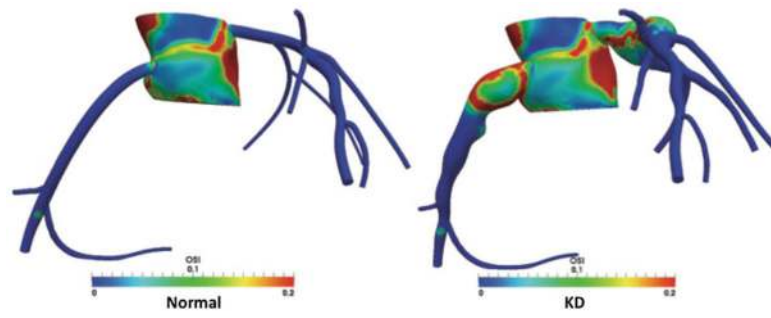
Fig. 6.
Comparison of OSI between the KD and normal models. Magnified view of the coronary arteries is shown
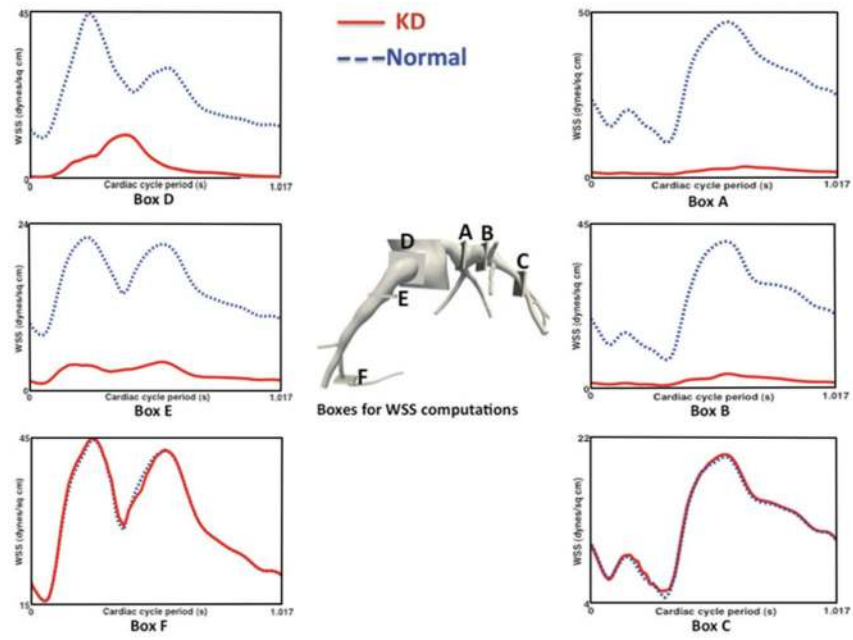
Fig. 7.
Comparison of time-varying and spatially averaged WSS for the KD and normal models at different locations in the RCA (*left column*, Boxes D–F) and LAD (*right column*, Boxes A–C)
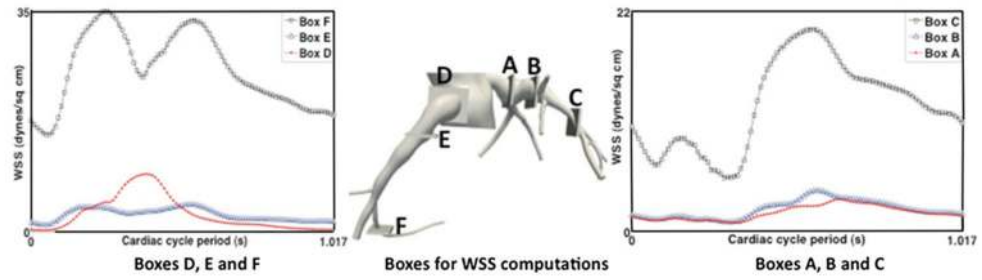
Fig. 8.
Comparison of the time-varying and spatially averaged WSS magnitude within the KD model at different locations in the LAD (*right*, Boxes A–C) and RCA (*left*, Boxes D–F)
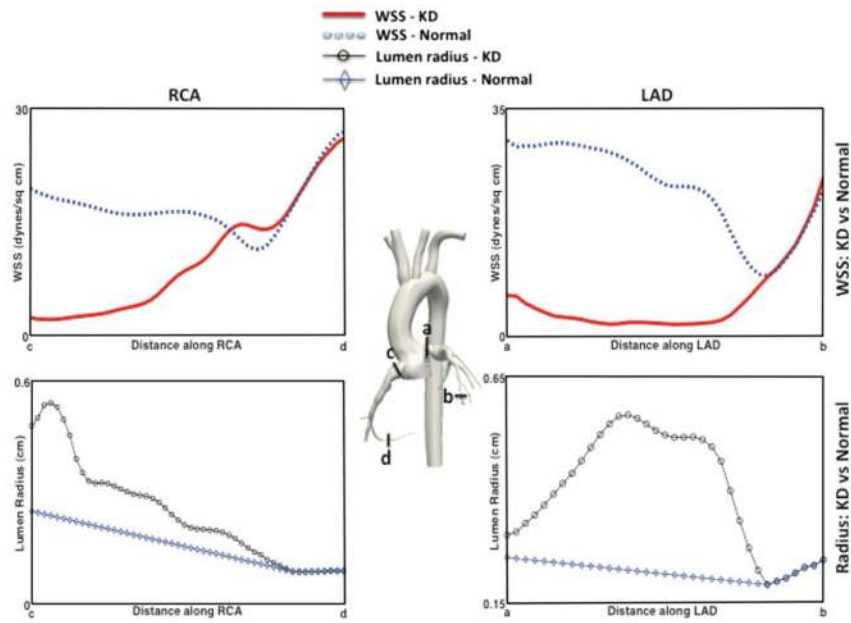
Fig. 9.
Comparison of mean WSS (*top row*) and Lumen Radius (*bottom row*) for the KD and normal models along the LAD (*right*) and RCA (*left*). In all plots, variation of parameters are obtained from points a to b in the LAD and c to d in the RCA, where distance is measured along the vessel centerline from the ostium
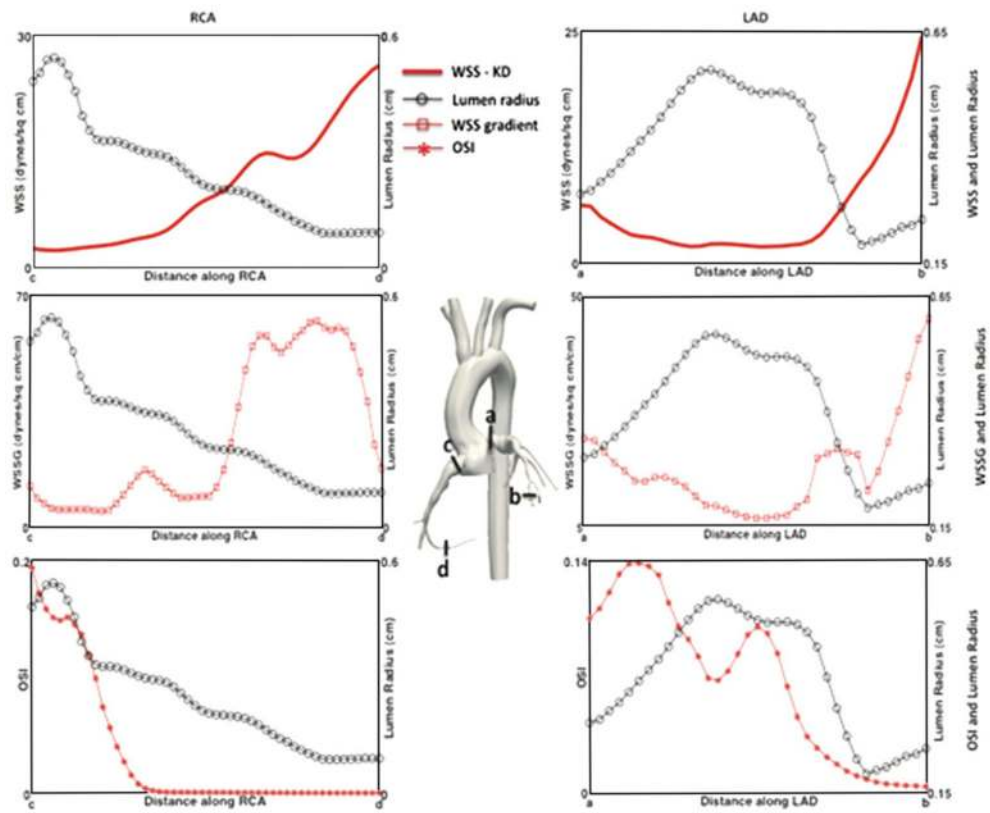
Fig. 10.
Variation of WSS and lumen radius for the KD model in the LAD (*top*, *right*) and RCA (*top*, *left*), variation of WSSG and lumen radius for the KD model in the LAD (*middle*, *right*) and RCA (*middle*, *left*), and variation of OSI and lumen radius for the KD model in the LAD (*bottom right*) and RCA (*bottom left*). In all the plots, variation of parameters are obtained from points a to b in the LAD and c to d in the RCA, where distance is measured along the vessel centerline from the ostium
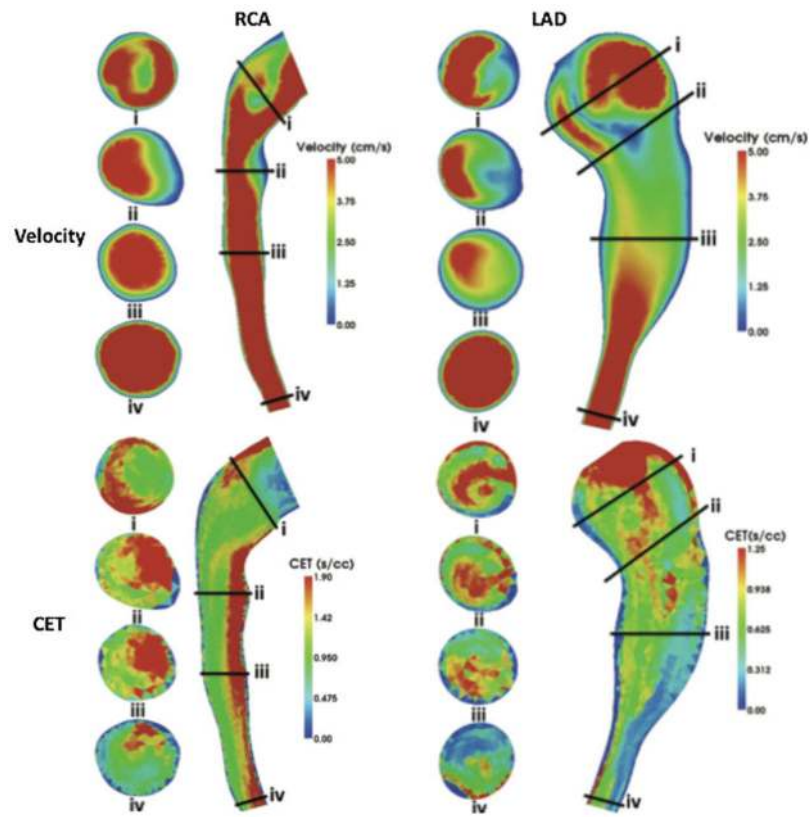
Fig. 11.
Velocity (*top row*) and CET (*lower row*) at different slices in the RCA (*left*) and LAD (*right*). Areas of high CET (*red*) generally correlate with areas of lower velocity (*blue*)
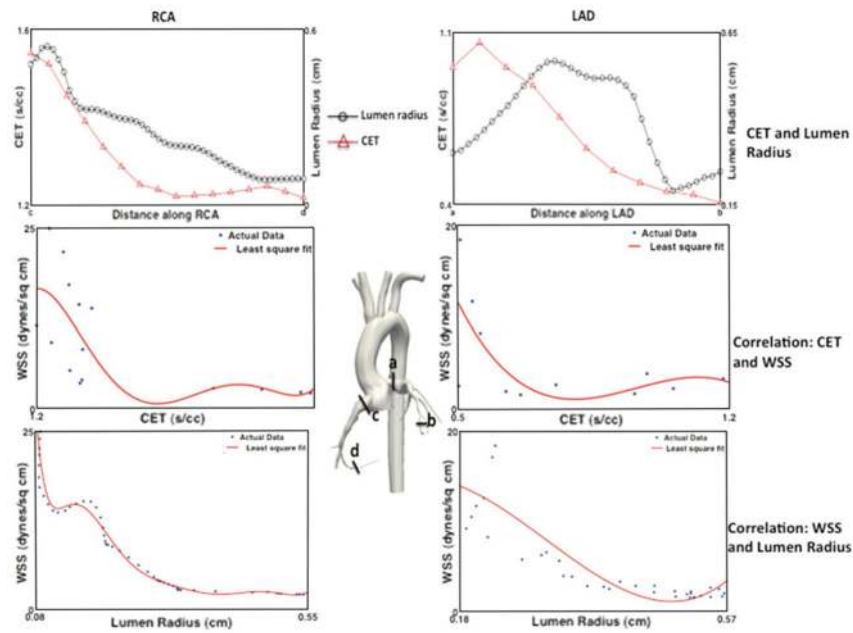
Fig. 12.
Variation of CET and lumen radius for the KD model in the LAD (*top right*) and RCA (*top left*), correlation of CET and mean WSS for the KD model in the LAD (*middle left*) and RCA (*middle right*), and correlation of lumen radius and mean WSS for the KD model in the LAD (*bottom left*) and RCA (*bottom right*). In all the plots, variation of parameters are obtained from points a to b in the LAD and c to d in the RCA, where distances are measured along the vessel centerline from the ostium
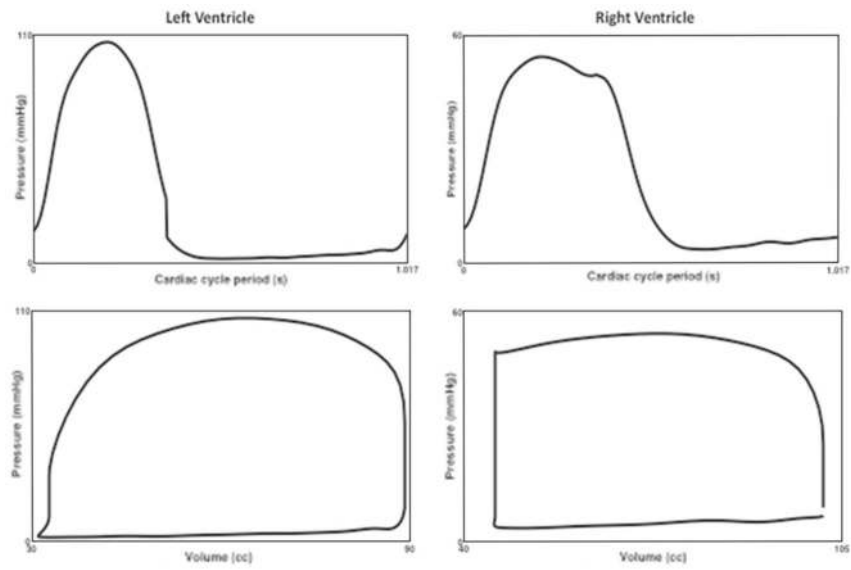
Fig. 13.
Left ventricular pressure (*top left*), right ventricular pressure (*top right*), left ventricular pressure-volume loop (*bottom left*), and right ventricular pressure-volume loop (*bottom right*)

Table 1

Flow data in LCA and RCA for the normal and KD simulations

	Mean LCA flow throughout the cardiac cycle (% of cardiac output)	Mean RCA flow throughout the cardiac cycle (% of cardiac output)	Total coronary flow throughout the cardiac cycle (% of cardiac output)	Mean LCA flow throughout the cardiac cycle (% of total coronary flow)	Mean RCA flow throughout the cardiac cycle (% of total coronary flow)
Normal	2.52	1.70	4.22	59.71	40.29
KD	2.76	1.72	4.48	61.60	38.40

Table 2

WSS and OSI values in normal and KD models

	Normal			KD		
	Mean	**Max**	**Min**	**Mean**	**Max**	**Min**
WSS: LAD (dynes/cm²)	27.15	40.10	11.36	3.81	4.52	0.05
WSS: RCA (dynes/cm²)	17.10	39.64	6.70	2.95	5.43	0.05
OSI: LAD	0.002	0.080	0.00	0.090	0.430	0.004
OSI: RCA	0.001	0.070	0.000	0.083	0.420	0.007